Steel and Composite Structures, *Vol. 31, No. 2* (*2019*) *149-158*
DOI: https://doi.org/10.12989/scs.2019.31.2.149

Mechanics of a variable damping self-centering brace: Seismic performance and failure modes

Xing-Si Xie [1], Long-He Xu [*1] and Zhong-Xian Li [2]

[1] *School of Civil Engineering, Beijing Jiaotong University, Beijing 100044, China*
[2] *Key Laboratory of Coast Civil Structure Safety of China Ministry of Education, Tianjin University, Tianjin 300072, China*

(*Received May 30, 2018, Revised March 1, 2019, Accepted March 20, 2019*)

Abstract. The force-deformation behavior, strain distribution and failure modes of a variable damping self-centering brace (VD–SCB) are theoretically analyzed, experimentally studied, and numerically simulated to guide its design. The working principle of the brace is explained by describing the working stages and the key feature points of the hysteretic curve. A large-scale brace specimen was tested under different sinusoidal excitations to analyze the recentering capability and energy dissipation. Results demonstrate that the VD–SCB exhibits a full quasi-flag-shaped hysteretic response, high ultimate bearing capacity, low activation force and residual deformation, and excellent recentering and energy dissipation capabilities. Calculation equations of the strain distribution in different parts of the brace are proposed and are compared with the experimental data and simulated results. The developments of two failure modes are compared. Under normal circumstances, the brace fails due to the yielding of the spring blocking plates, which are easily replaced to restore the normal operating conditions of the brace. A brief description of the design procedure of the brace is proposed for application.

Keywords: self-centering brace; variable damping; hysteretic response; strain distribution; failure mode

1. Introduction

Modern structural design is gradually shifting from strength-based methods to performance-based design. High safety rating and good reliability are the primary requirements of future structures. Earthquake resilient structures have become an important aspect of high-performance structural systems due to their excellent seismic performance and recentering capability. These structures are capable of quick recovery of the normal use functions after an earthquake because replaceable or self-centering members are used to prevent residual deformation. The self-centering brace (SCB) is developed from the buckling-restrained brace (BRB). It exerts a sufficient recentering capability on the structure because of its own prestressing force. By using SCBs, the residual deformation angle is reduced to 0.005 rad or less, thereby ensuring that the repair cost does not exceed the reconstruction cost (McCormick *et al.* 2008).

Many materials have been used for SCBs to guarantee their recentering capability. Christopoulos *et al.* (2008) proposed a high-capacity pre-tensioned tendon (PT) SCB to improve the performance of conventional braces in buildings. The PT–SCB exhibits full recentering behaviors during cyclic tests with an equivalent drift ratio of 1.5%; an external friction fuse ensures stable and smooth responses even at an approximately 3.0% drift ratio (Erochko *et al.* 2015a, b). Miller *et al.* (2012) added shape memory alloy (SMA) rods to a BRB for presenting a SMA–SCB. Large-scale tests demonstrated that the SMA–SCB provides a stable force-displacement response with significant dissipative energy, and good recentering and deformation capability (Eatherton *et al.* 2014). Chou and Chung (2014) theoretically and experimentally investigated a new dual-core PT–SCB with a flag-shaped hysteretic response. The brace exhibits excellent performance with a 2% drift ratio at an ultimate axial force of 1400 kN and also survives low-cycle fatigue tests at a 1.5% drift ratio (Chou and Chung 2015, Chou *et al.* 2016). Wang *et al.* (2017) proposed a refined PT–SCB, in which a cross anchor ensures adequate deformation of the PTs and the entire SCB. Xu *et al.* (2016a) developed a pre-pressed disc-spring SCB that combines disc springs for recentering with friction plates for energy dissipation. The quasi-static test results demonstrated that the bracing system exhibits stable and repeatable recentering hysteretic responses with effective energy dissipation (Xu *et al.* 2016b). In the past decade, many researches have introduced various SCBs that effectively reduce the residual deformation of structures (Ma and Yam 2011, Ozbulut and Hurlebaus 2012, Zhou *et al.* 2014, Kitayama and Constantinou 2016, Xie *et al.* 2016, Abou-Elfath 2017, Choi *et al.* 2017, Chi *et al.* 2018).

From the perspective of working principle, the residual deformation of the structure can be prevented, only when the recentering capability of the SCB is greater than the dissipative energy. However, this means that the damping of the SCB is significantly lower than that of the BRB, which affects the ability of the SCB to control structural vibration. The stiffness change when activation also significantly

*Corresponding author, Professor,
E-mail: lhxu@bjtu.edu.cn

ISSN: 1229-9367 (Print), 1598-6233 (Online)

influences the stiffness of the entire structure and amplifies the displacement responses during earthquakes. Xu *et al.* (2018) developed a variable damping (VD) SCB to reduce the activation force and sudden change in stiffness when activation. Results showed that the VD–SCB exhibits a full quasi-flag-shaped force-displacement behavior, with a small stiffness change and a low axial force when activation. The mechanics of the VD–SCB, in particular, the strain distribution and failure modes, still require further analysis to clarify and improve the ultimate seismic performance.

In this paper, the mechanics and working principles of the VD–SCB are explained. Cyclic tests of a large-scale VD–SCB specimen were carried out under different sinusoidal excitations to analyze its force-deformation behaviors. The strain distribution equations of the brace are validated using experiments and numerical simulations. The simulated development processes of two failure modes are compared with the experimental results. A design procedure of the VD–SCB is proposed for practical application.

2. Hysteretic behavior of the VD–SCB

2.1 Working principle

The recentering capability of the VD–SCB is provided by disc springs, and a magnetorheological fluid (MRF) is used to dissipate most of the energy. A piston and three permanent magnets are installed at the middle of the inner tube, with which a cylinder and two sealing blocking plates form a closed magnetic circuit together. The disc springs and four spring blocking plates are always compressed at both sides of the piston, and two outer tubes are attached to the cylinder with clamps. The recentering and energy dissipation members are connected in parallel and are hinged by the connection plates at both two ends of the VD–SCB. The configuration of the VD–SCB is shown in Fig. 1.

Fig. 2 shows the operation of the VD–SCB that consists of seven steps. At the beginning of loading, the brace elongates elastically with the series stiffness k_1 of the inner and outer tubes. When the restoring force exceeds the activation force of the brace, the inner and outer tubes move relative to each other. The integral stiffness changes from k_1 to the sum of the disc-spring stiffness k_{DS} and the change rate of the damping force. As the deformation ratio increases, the damping force reaches the maximum; at this time, the integral stiffness of the VD–SCB is equal to the disc-spring stiffness k_{DS}. When the axial deformation reaches its maximum level and begins to decrease, the restoring force decreases immediately by twice the amount of the ultimate damping force; at this time, there is no relative movement between the inner and outer tubes. Subsequently, the VD–SCB unloads, and the brace stiffness is the sum of the disc-spring stiffness k_{DS} and the change rate of the damping force. Finally, the brace recovers as the elastic deformation disappears. The operating stages of tension and compression are the same for the VD–SCB. The restoring force F is given as

$$F=\begin{cases} k_1\Delta & 0\le\Delta<\Delta_{A,loading} \text{ and } \Delta\cdot\dot{\Delta}\ge 0 \\ k_{DS}\left(\Delta-\Delta_{A,loading}\right)+P+f & \Delta_{A,loading}\le\Delta<\Delta_{V,loading} \text{ and } \Delta\cdot\dot{\Delta}\ge 0 \\ k_{DS}\left(\Delta-\Delta_{A,loading}\right)+P+f_{Max} & \Delta_{V,loading}\le\Delta<\Delta_{Max} \text{ and } \Delta\cdot\dot{\Delta}\ge 0 \\ k_{DS}\left(\Delta_{Max}-\Delta_{A,loading}\right)+P+f_{Max}\left(1-2\dfrac{\Delta_{Max}-\Delta}{\Delta_{Max}-\Delta_{A,unloading}}\right) & \Delta_{A,unloading}<\Delta\le\Delta_{Max} \text{ and } \Delta\cdot\dot{\Delta}\le 0 \\ k_{DS}\left(\Delta-\Delta_{A,loading}\right)+P-f_{Max} & \Delta_{V,unloading}<\Delta\le\Delta_{A,unloading} \text{ and } \Delta\cdot\dot{\Delta}\le 0 \\ k_{DS}\left(\Delta-\Delta_{Recentering}\right)+P-f & \Delta_{Re}<\Delta\le\Delta_{V,unloading} \text{ and } \Delta\cdot\dot{\Delta}\le 0 \\ k_1\Delta & 0\le\Delta<\Delta_{Recentering} \text{ and } \Delta\cdot\dot{\Delta}\ge 0 \end{cases} \quad (1)$$

where P is the pre-pressed force of disc spring, f is the damping force, f_{Max} is the ultimate damping force, Δ and $\dot{\Delta}$ are the deformation ratio and velocity of the VD–SCB, respectively. $\Delta_{A,loading}$, $\Delta_{A,unloading}$, $\Delta_{V,loading}$, $\Delta_{V,unloading}$, Δ_{Max} and $\Delta_{Recentering}$ are the deformation ratios at the key feature

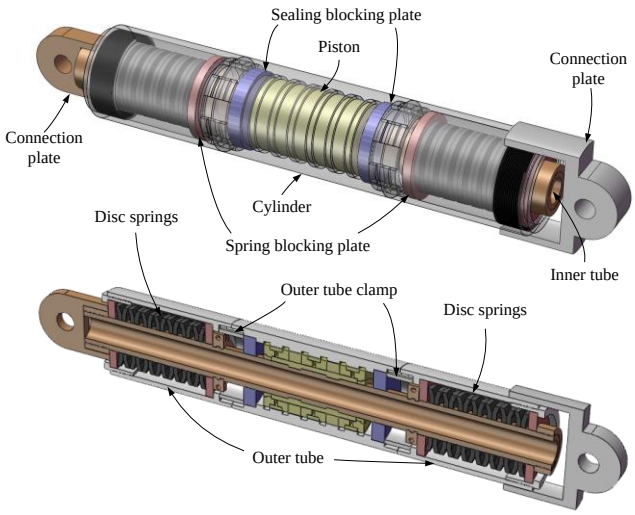

Fig. 1 Configuration of the VD–SCB

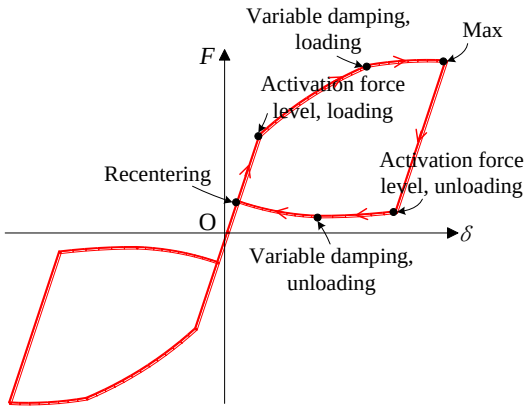

Fig. 2 Operation and key feature points of the VD–SCB

Table 1 Design parameters of the specimen and the disc spring

Design parameter		Value (mm)
Specimen	Inner tube	ϕ110×13.5
	Cylinder	ϕ277×27/35.5
	Outer tube	ϕ277×14.5
	Thickness of spring blocking plate	25
	Thickness of sealing blocking plate	40
Disc spring	Outer diameter	200
	Inner diameter	112
	Height	16.2
	Thickness	11.25
	Solid height	4.95

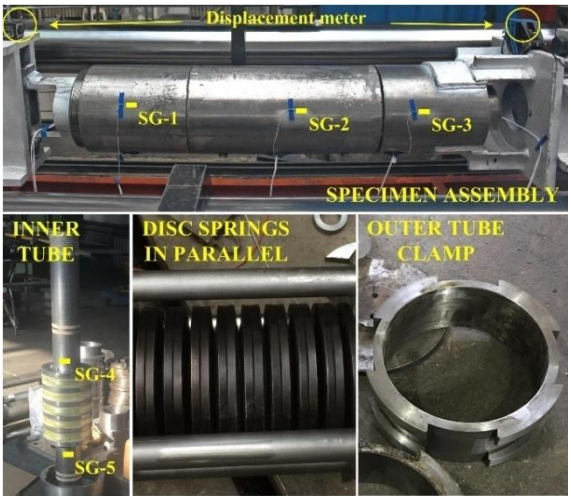

Fig. 3 VD–SCB Specimen

points of the hysteretic curve shown in Fig. 2, where the superscripts A and V represent the activation force level and variable damping, respectively.

2.2 Force-deformation responses

A large-scale 1.365 m VD–SCB specimen, as shown in Fig. 3 (SG represents the strain gauge), was tested under the sinusoidal excitations with different frequencies and amplitudes. The specimen was hinged with the test machine by the clevis pins. Table 1 lists the design parameters of the VD–SCB specimen and the disc spring used for recentering. Fig. 4 shows the multi-level sinusoidal loading history; the seven target axial deformation ratios are 0.30%, 0.55%, 0.80%, 1.05%, 1.35%, 1.60%, and 1.85%. The axial deformation ratio is the ratio of the axial deformations of the brace to the total length. In previous tests (Xu *et al.* 2016a, 2018), the responses of the disc springs and MRF were investigated, as shown in Fig. 5. The disc springs exhibit a linear force-displacement behavior and are compressed with a stiffness of k_{DS} after the force reaches

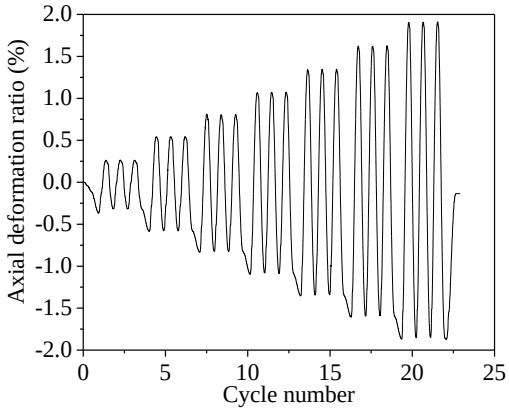

Fig. 4 Multi-level sinusoidal loading history

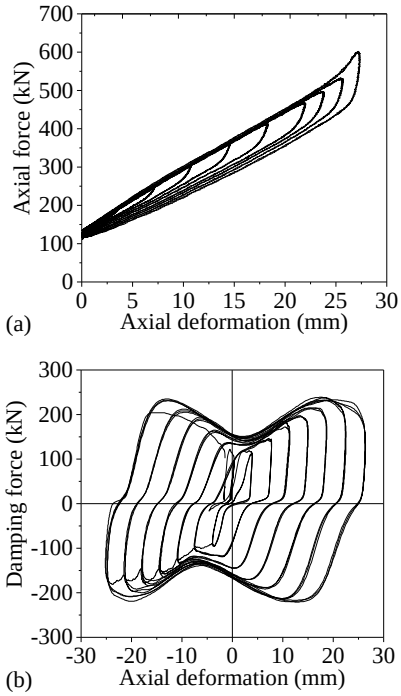

Fig. 5 Force-deformation behaviors of the (a) disc springs and (b) MRF

the pre-pressed force. The MRF provides variable damping force during cyclic loading. The initial damping force is 105 kN. The damping force increases as the axial deformation increases, and stabilizes after reaching 220 kN.

The force-deformation behaviors of the VD–SCB with P = 115 kN and k_{DS} = 3.68 kN/mm under sinusoidal excitations are shown in Fig. 6. Full quasi-flag-shaped curves are observed and the VD–SCB exhibits high ultimate bearing capacity, low activation force and residual deformation, and excellent recentering and energy dissipation capabilities. Since the test specimen is connected to the testing machine by the hinged connection plates, the machining error of the clevis pins causes the specimen to stagger, resulting in a 0.2% deformation ratio during the tension and compression transformation. This resulted in errors in the displacement meter measurement and the residual deformation data. Therefore, there are differences in the shape of the

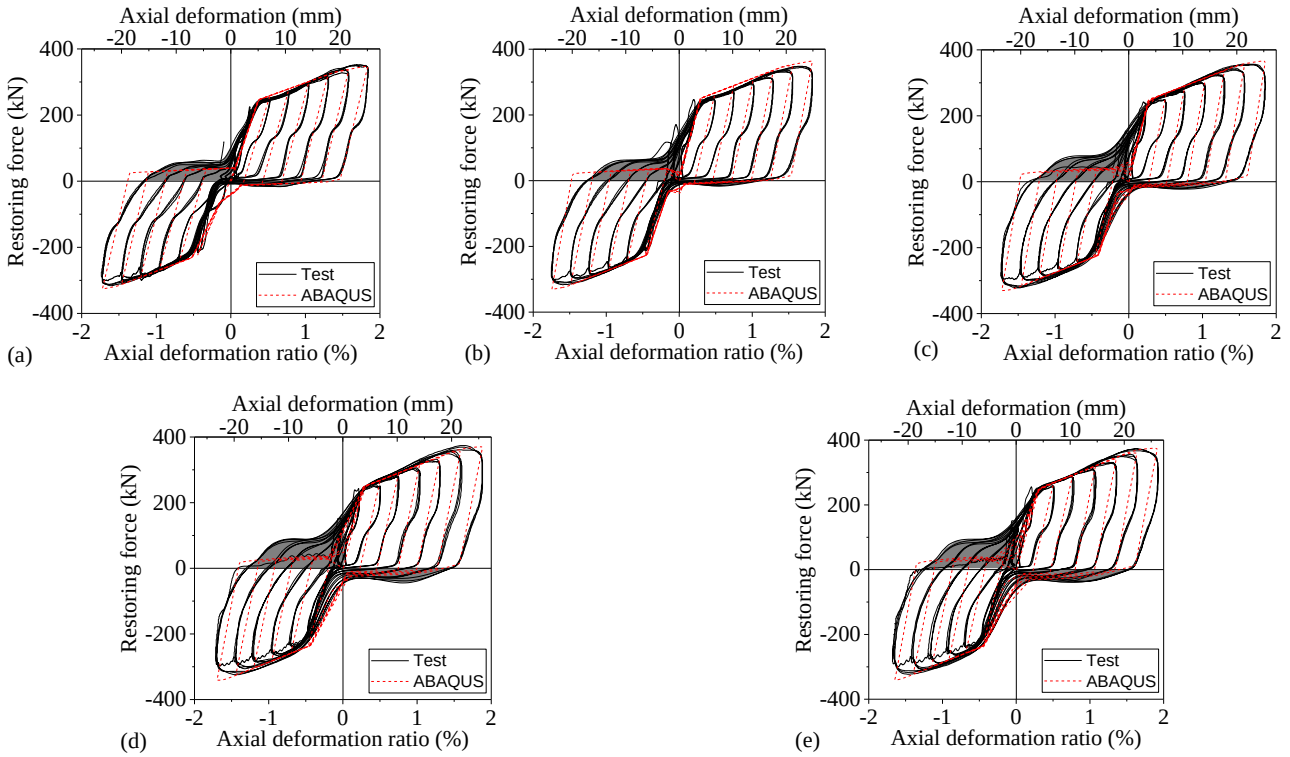

Fig. 6 Force-deformation behaviors of the VD–SCB under sinusoidal excitations with frequencies of (a) 0.05 Hz, (b) 0.1 Hz, (c) 0.2 Hz, (d) 0.3 Hz, and (e) 0.4 Hz

hysteretic curve between the tension and compression stages, which affects the symmetric behavior of the seismic performance. By improving the configuration of the connection, the stagger of the clevis pins can be reduced, thereby improving the recentering capability of the brace.

In order to compare the energy dissipation capability in tension and compression, the brace behavior is separated into tension and compression behaviors. The equivalent viscous damping ratio ξ_{eq} is used to evaluate the energy dissipation of the VD–SCB

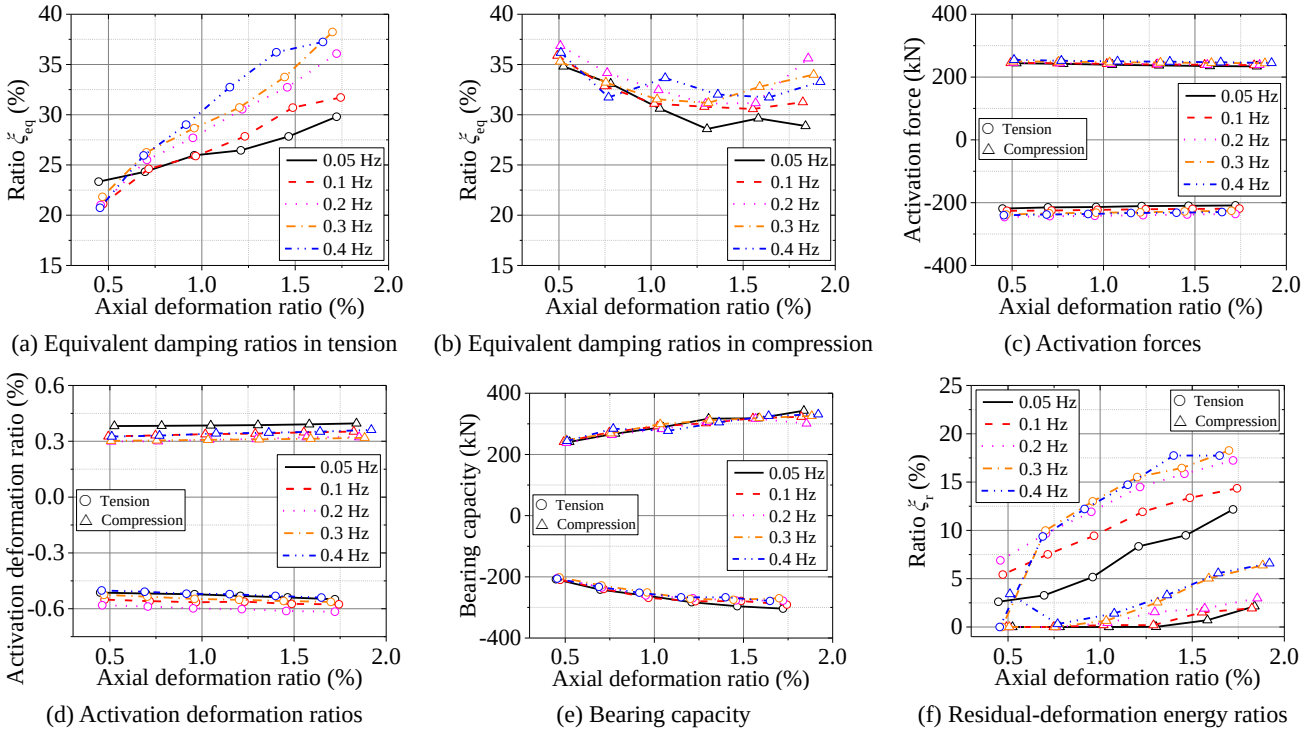

Fig. 7 Seismic performances of the VD–SCB with P = 115 kN and k_{DS} = 3.68 kN/mm

$$\xi_{eq} = \frac{E_D}{4\pi E_{so}} \times 100\% = \frac{E_H}{2\pi E_{so}} \times 100\% \quad (2)$$

where E_D is the dissipative energy, E_{SO} is the ultimate elastic strain energy, and E_H is the dissipated energy during tension or compression. The energy dissipation is proportional to ξ_{eq}. Figs. 7(a) and (b) show the ratios ξ_{eq} of the VD–SCB in tension and compression; opposite trends of the ratio ξ_{eq} versus the deformation ratio relationship are observed. For the VD–SCB in compression, the ratio ξ_{eq} decreases as the axial deformation ratio increases when the axial deformation ratio is less than 1.25%. As the deformation ratio further increases, the ratio ξ_{eq} increases from 27.5% to 37.5%. This can be regarded as the normal change law of ratio ξ_{eq}. Because of the stagger of the clevis pins, the restoring force of the VD–SCB in tension reverses earlier, resulting in a significant increase in energy dissipation. The brace was also not loaded to the specified deformation ratio. The ratios ξ_{eq} for small deformations are much lower than those in compression, and it increases continuously as the axial deformation ratio increases. Since the MRF is a material with rheological properties, the viscous damping results in an increase in the ratio ξ_{eq} as the loading frequency increases, regardless of whether the brace experiences tension or compression.

The restoring forces and axial deformation ratios during loading activation, which represent one of the key feature points of the curve, are shown in Figs. 7(c) and (d). The activation force and activation deformation ratio of the brace are quite stable and do not change significantly with the axial deformation ratio; the average values are 245 kN and 0.34% in compression, 232 kN and 0.55% in tension, respectively. Since the damping force provided by the MRF is proportional to the velocity, the activation force increases slightly as the loading frequency increases. The energy dissipation during the activation of the VD–SCB is still relatively small; therefore, the influence of the frequency on the activation force is negligible. The activation deformation ratio during compression is 0.20% less than that during tension, which corresponds to the clevis pin stagger and represents a measurement error. The real activation deformation ratios during tension and compression are symmetrical.

When the axial deformation ratio reaches the maximum, the VD–SCB experiences the ultimate bearing capacity, as shown in Fig. 7(e). The bearing capacity of the brace exhibits a linear growth trend when the deformation ratio is less than 1.25%, and the growth rate decreases as the deformation ratio increases. The reason for the change in stiffness is related to the working principle of the SCB. A continuous and slow change in stiffness is more favorable in terms of structural response and effectively reduces the nonlinear displacement of the SCB structure. Because the velocity of sinusoidal loading is 0 mm/s at the ultimate axial deformation ratio, the viscous damping force disappears, and the bearing capacity of the VD–SCB does not change with the increase in loading frequency. The ultimate bearing capacities are 320 kN at a compression deformation ratio of 1.85% and 295 kN at a tension deformation ratio of 1.75%.

The residual-deformation energy ratio ξ_r is used to evaluate the recentering capability of the VD–SCB

$$\xi_r = \frac{E_r}{E_H} \times 100\% \quad (3)$$

where E_r is the dissipative energy when residual deformation occurs, as shown by the shades in Fig. 6. The recentering capability is inversely proportional to ξ_r. Fig. 7(f) shows the ratios ξ_r of the VD–SCB. An unexpected defect in machining accuracy leads to the stagger of the clevis pins, thus a substantial increase in the dissipative energy when residual deformation occurs during tension, resulting in a ratio ξ_r of up to 18.3%. However, the actual residual-deformation energy dissipation of the brace specimen should be similar to that during compression and no more than 7.5%. The ratio ξ_r of the brace increases as the axial deformation ratio and loading frequency increase. Since this effect is not fully taken into account, the pre-pressed force is insufficient and a small amount of residual deformation occurs. Because a properly designed brace should ensure that the residual deformation is completely eliminated, the disc-spring pre-pressed force P and stiffness k_{DS} of the brace in current cases should be further increased so that the ratio ξ_r can be reduced to 0, thereby completely preventing the residual deformation of the VD–SCB.

2.3 Finite element analysis

In order to analyze the strain distribution and failure mode of the VD–SCB, an ABAQUS finite element model of the test specimen was established using the C3D8 solid elements, as shown in Fig. 8. An elastic-perfectly plastic model with a yield stress of 355 MPa and Young's modulus of 210 GPa was used as the constitutive model of steel. The disc springs were simulated using the spring-damping elements with a damping coefficient of 0. The sinusoidal loadings corresponding to the test cases in Fig. 6 were used in the finite element model.

The comparisons of the simulated restoring forces F_s and restoring forces in tests F_e at each target deformation

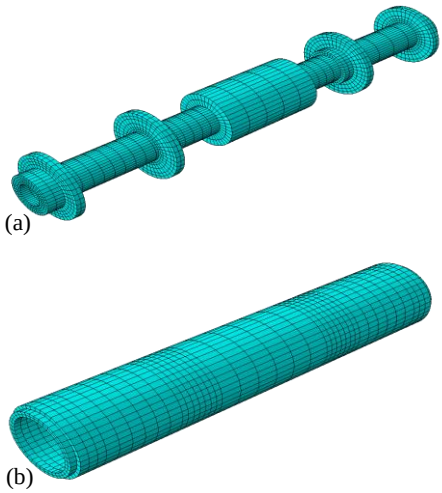

Fig. 8 Finite element model of (a) the inner tube, piston and plates, and (b) the outer tube and cylinder

Table 2 Comparisons of restoring forces at different target deformation ratios

Axial deformation ratio (%)		F_s/F_e				
		0.05 Hz	0.1 Hz	0.2 Hz	0.3 Hz	0.4 Hz
Brace in tension	0.55	1.08	1.05	1.03	0.99	1.07
	0.8	1.02	1.05	1.03	1.08	1.09
	1.05	1.02	1.01	1.04	1.07	1.08
	1.35	1.02	1.06	1.05	1.08	1.07
	1.6	1.05	1.08	1.07	1.09	1.06
	1.85	1.07	1.08	1.07	1.09	1.07
Brace in compression	0.55	1.07	1.07	1.06	1.08	1.03
	0.8	1.04	1.07	1.04	1.04	1.02
	1.05	1.04	1.06	1.04	1.06	1.04
	1.35	1.02	1.06	1.06	1.04	1.06
	1.6	1.06	1.07	1.04	1.06	1.05
	1.85	1.02	1.07	1.06	1.05	1.05

ratio are shown in Table 2. The maximum ratios of the forces F_s and F_e are 1.08, 1.08, 1.07, 1.09 and 1.09 respectively under sinusoidal excitations with frequencies of 0.05 Hz, 0.1 Hz, 0.2 Hz, 0.3 Hz and 0.4 Hz, whereas the minimum ratios are 1.02, 1.01, 1.03, 0.99 and 1.02 respectively. Fig. 6 also shows the comparison of force-deformation behaviors between the simulation results and experimental data under the sinusoidal excitations. Good agreements are observed for the simulation and experimental tests; therefore, the model can be used for the strain and failure analyses. It is worth noting that although the stagger of the clevis pins is considered, the simulation results still do not fully describe the force-deformation behavior of the VD–SCB during the unloading stages in tension, resulting in slightly lower values of the simulated energy dissipation. Because the strain and failure analyses mainly focus on the limit state of the brace, the numerical simulation errors during unloading can be ignored.

3. Strain distribution of the VD–SCB

The purpose of the strain distribution analysis is to obtain the mechanics of different parts of the VD–SCB, and then determine the design requirements of each part based on the force-deformation behavior of the entire brace.

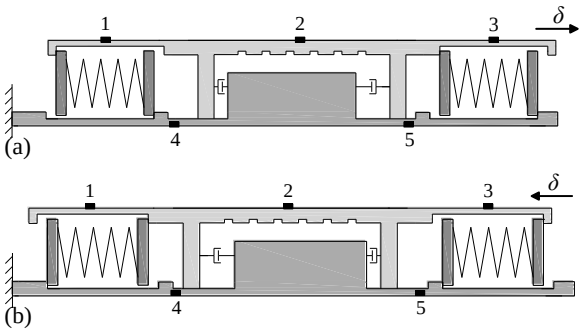

Fig. 9 Working states of the VD–SCB (a) in tension and (b) in compression

The VD–SCB exhibits different mechanical characteristics at each section of the inner and outer tubes during tension and compression, causing different strain distributions. Fig. 9 shows the working states of the brace in tension and compression.

The strains ε_n (n = 1, 2, 3, 4, 5) at each section of the inner and outer tubes are obtained as follows

$$\varepsilon_1 = \begin{cases} \dfrac{T_{\text{DS-1}}}{A_1 \cdot E} & \Delta \le 0 \\ 0 & \Delta > 0 \end{cases} \tag{4}$$

$$\varepsilon_2 = \frac{T_{\text{DS-1}} + \eta f}{A_2 \cdot E} \tag{5}$$

$$\varepsilon_3 = \begin{cases} \dfrac{T_{\text{DS-1}} + f + T_{\text{DS-2}}}{A_3 \cdot E} & \Delta \le 0 \\ \dfrac{T_{\text{DS-1}} + f}{A_3 \cdot E} & \Delta > 0 \end{cases} \tag{6}$$

$$\varepsilon_4 = \frac{T_{\text{DS-2}} + f}{A_4 \cdot E} \tag{7}$$

$$\varepsilon_5 = \frac{T_{\text{DS-2}}}{A_5 \cdot E} \tag{8}$$

where $T_{\text{DS-1}}$ and $T_{\text{DS-2}}$ are the forces of the left and right disc springs (Fig. 9), A_n is the axial cross-sectional area, and E is Young's modulus of steel. η ($0 \le \eta \le 1$) is the proportion of the damping forces on both sides of the piston, which has to be determined by further experiments; commonly, a value of 1.0 is used in the design for safety purposes.

Fig. 10 shows the strain-deformation behaviors of the VD–SCB with P = 115 kN and k_{DS} = 3.68 kN/mm under sinusoidal excitation with a frequency of 0.05 Hz. The disc springs are only installed on the left side, which means that the force $T_{\text{DS-2}}$ = 0. Three strain gauges were arranged on the outer tube and cylinder of the test specimen, as shown in Fig. 3; these correspond to strains ε_1, ε_2 and ε_3. The strain ε_1 remains 0 in compression, and increases as the axial deformation ratio increases in tension. When the brace is in tension, the strain ε_1 corresponds to stiffness k_1 before activation, and to stiffness k_{DS} after activation. The strain ε_2 exhibits a quasi-flag shape, but its envelope area is different in tension and compression due to the different proportions η of the damping forces on the left side of the piston. The shape of the strain-deformation curve for the strain ε_3 is the same as that of force-deformation curve of the entire brace, as shown in Fig. 10(c). The trends of the strain change are the same as those of the theoretical results obtained by Eqs. (4)-(6). In addition, good agreements are also observed between the simulated and experimental results.

As shown in Fig. 10(a), although the strain change trend at SG-1 is consistent with that of the theoretical result, there are many abnormal segments in the curve. A comparison of the strain and axial deformation ratio history curves at SG-1 (Fig. 11) indicates that the strain measurement result shows

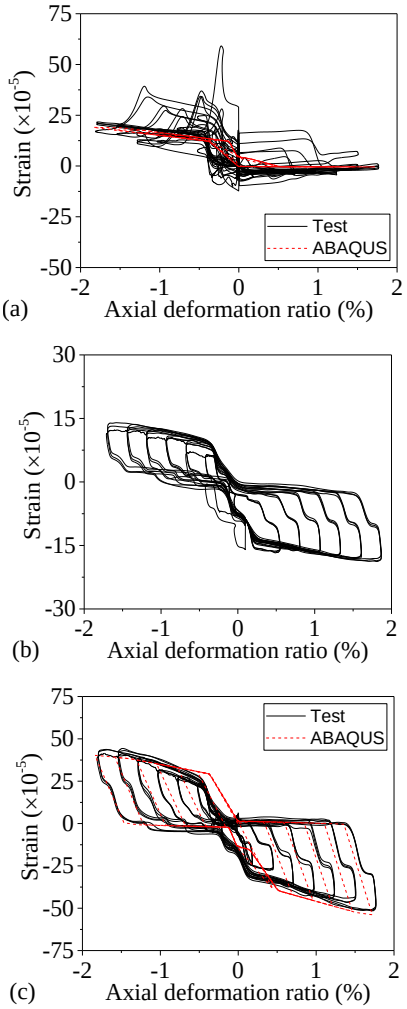

Fig. 10 Strain-deformation behaviors of the VD–SCB at (a) SG-1, (b) SG-2 and (c) SG-3

several sharp peaks at the same moment in each cycle; the values are much larger than those of the normal strain range. These peaks correspond to the time when the brace is unloaded during tension, as shown in Fig. 10(a); therefore, the reason for this phenomenon may be the stagger of the clevis pins. A comparison of Fig. 10(a) and (b)-(c) indicates that the influence of the clevis pin stagger on the test results is much smaller for SG-2 than SG-1, whereas SG-3 is completely unaffected; this demonstrates that the rigid and hinged connections only significantly disturb the strain distribution measurement of the left outer tube.

4. Failure mode of the VD–SCB

4.1 Mode I

To verify the fatigue property of the brace, a fatigue test of the VD–SCB was conducted. According to the Chinese code JGJ 297-2013, the energy dissipation capability of the brace cannot change by more than 15% in 30 cycles. During the fatigue test, the VD–SCB specimen with P = 115 kN and k = 8.59 kN/mm was continuously loaded and unloaded under 0.2 Hz sinusoidal excitation at 1.85% deformation

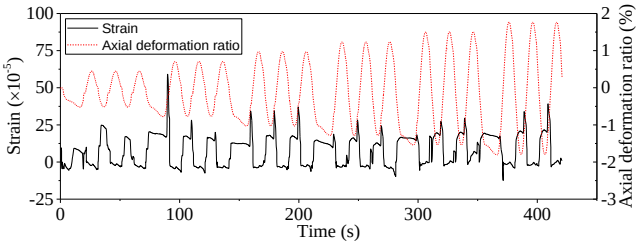

Fig. 11 Strain and axial deformation ratio history curves of the VD–SCB at SG-1

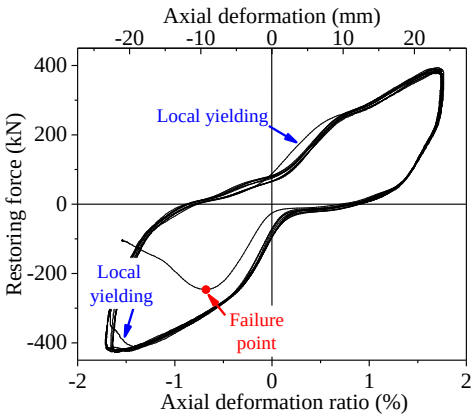

Fig. 12 Force-deformation behavior of the VD–SCB under 0.2 Hz sinusoidal excitation

ratio. An unexpected failure mode occurs in the 41st cycle. The clamp of the outer tube is damaged, resulting in the loss of the bearing capacity of the brace.

The force-deformation behavior of the brace from the 31st to 41st cycles is shown in Fig. 12. The locking design of the clamp lacks reliability, resulting in gradual loosening during the fatigue test. In the 40th cycle, when the brace reaches the target deformation ratio, the clamp undergoes local yielding. During the 40th compression cycle, yielding of the clamp occurs. In the 41st tension cycle, the plastic deformation of the clamp increases significantly due to further loosening, and the brace loses all bearing capacity.

The damaged clamp is shown in Figs. 13(a) and (b). The remaining stress area is 30% to 40%, and obvious bending damage is observed at the base of the clamp. The numerical simulation of this failure mode indicates that the stress is concentrated at the base because of the reduction of stress area as shown in Fig. 13(c); this results in the strain exceeding the yield limit of the steel used for the specimen.

4.2 Mode II

The failure mode I of the VD–SCB is not an ideal mode and should be avoided in practical application. The occurrence of this failure mode does not mean that the brace cannot possess good fatigue properties. In order to analyze the failure mode when the clamp is not loosened, the numerical model of the brace with $P = 115$ kN and $k_{DS} = 8.59$ kN/mm is simulated under monotonic tension excitation with a velocity of 5 mm/s.

Fig. 14 shows the force-deformation behavior of the

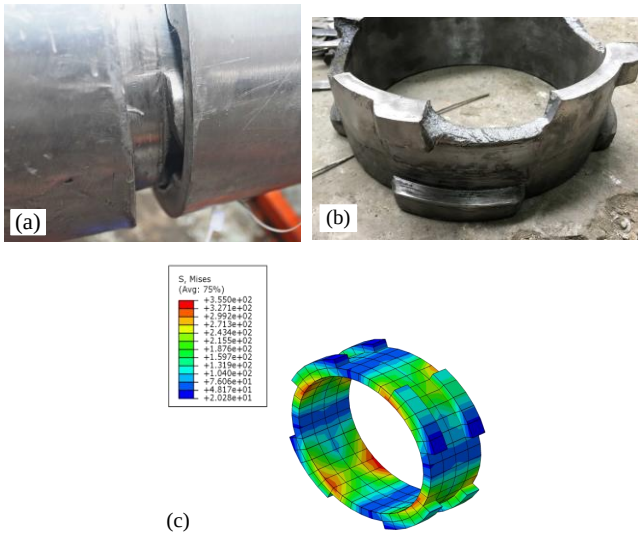

Fig. 13 Clamp damage when (a) tested, (b) disassembled and (c) simulated

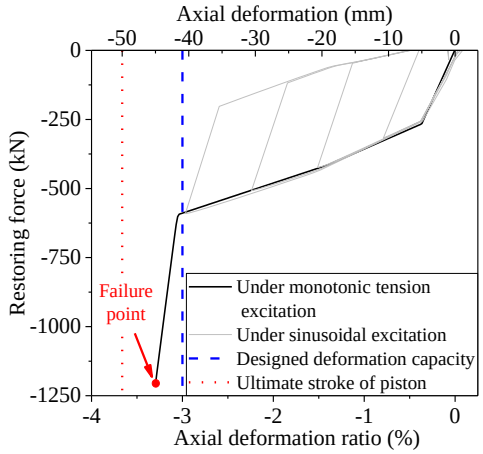

Fig. 14 Force-deformation behavior of the VD–SCB under monotonic tension excitation

brace. Force-deformation behavior of the VD–SCB when the axial deformation ratio exceeds 1.85% is simulated. Regardless whether the brace is subjected to small or large axial deformation, full quasi-flag-shaped hysteretic curves without full compression of the disc springs are observed; this is consistent with the working principle of the brace. The designed deformation capacity of the test specimen is 3.00% of the total length of the brace, and the ultimate stroke of the piston is 3.70% of the total length. When the deformation ratio of the brace is smaller than its design value, the disc springs and MRF operate normally, and the simulated curve agrees well with the experimentally obtained skeleton curve of the brace. When the deformation ratio exceeds 3.00%, the disc springs are completely pressed, leading to a sudden increase in the brace stiffness and bearing capacity. The brace is ultimately damaged when the deformation ratio reaches 3.30% and the ultimate bearing capacity is 1205 kN. At this time, the piston still does not reach the ultimate stroke, which ensures that the MRF can be used repeatedly without loss of energy

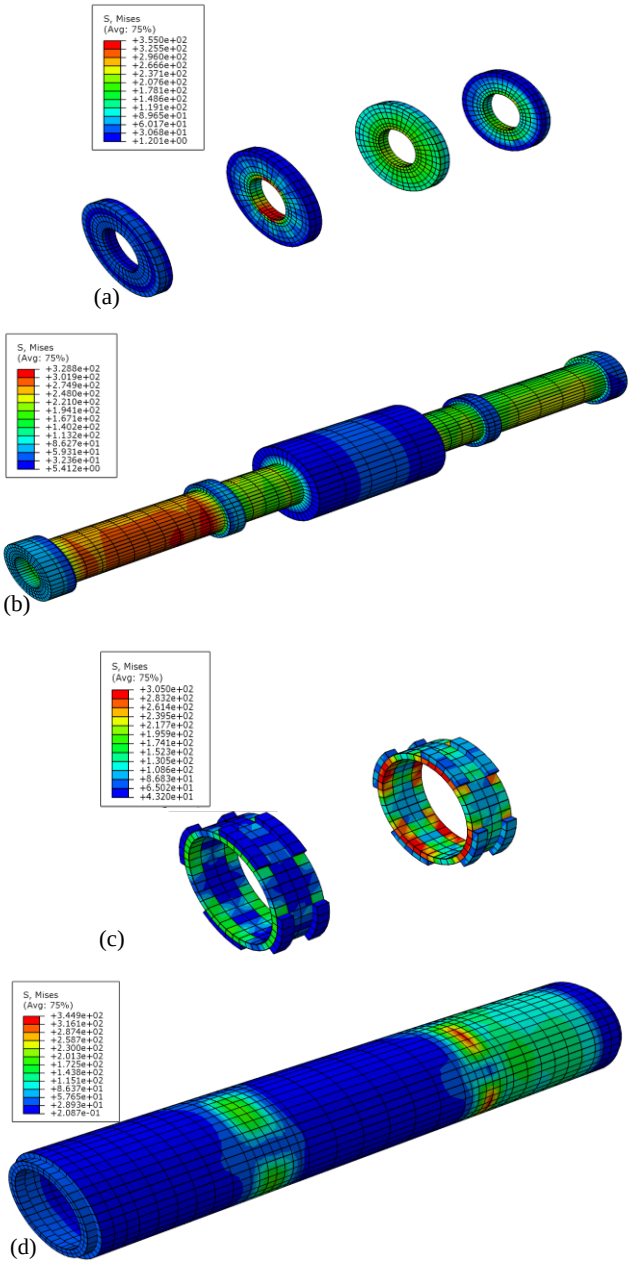

Fig. 15 Stress of the (a) spring blocking plates, (b) inner tube and piston, (c) clamp of outer tube, and (d) outer tube and cylinder

dissipation capacity, provided that an appropriate maintenance and replacement schedule is observed.

The stress distributions of the damaged brace are shown in Fig. 15. The spring blocking plates undergo local yielding, whereas the inner and outer tubes, pistons, cylinders and clamps are only elastically deformed. The ultimate stress values of the inner tube and piston, clamps, and outer tube and cylinder are 329 MPa, 305 MPa and 345 MPa, respectively. Compression, tension and shear performance checks should be carried out at the locations of high stress. The positions on the inner tube corresponding to the local yielding points of the spring blocking plates do not yield. This indicates that this failure mode is characterized by the yielding of the spring blocking plates because of the

completely pressed disc springs. Only the spring blocking plates need to be replaced to restore the normal operating conditions of the brace; this demonstrates the superiority of the earthquake resilient structural component in post-earthquake repair.

5. Brief description of the design process of the VD–SCB

The design procedure of the VD–SCB is summarized as follows:

(1) Determine $F_{\mathrm{A,loading}}$ (the sum of the pre-pressed force P and initial damping force $f_{\mathrm{A,loading}}$) and $\Delta_{\mathrm{A,loading}}$ based on the performance level of the braced structure under frequent ground motion; determine F_{Max} and Δ_{Max} based on the performance level of the braced structure under very rare ground motion.

(2) Determine the variable damping region R as

$$R=\frac{1}{2}\left(\Delta_{\mathrm{V,loading}}-\Delta_{\mathrm{A,loading}}+\Delta_{\mathrm{V,unloading}}-\Delta_{\mathrm{Recentering}}\right) \quad (9)$$

The region R should be first selected empirically, and then optimized using several structural analyses after completing step (4).

(3) Determine the safety factor β of the brace ($\beta \geq 1.0$), the forces P and $f_{\mathrm{A,loading}}$ are obtained as

$$\begin{cases} P=\beta\cdot f_{\mathrm{A,loading}} \\ F_{\mathrm{A,loading}}=P+f_{\mathrm{A,loading}} \end{cases} \quad (10)$$

The factor β can be selected to be larger than 1.2 to consider the influence of the axial deformation ratio and loading frequency, ensuring the residual deformation of the brace within an acceptable range.

(4) The damping force change rate is expressed as

$$\frac{f_{\mathrm{Max}}-f_{\mathrm{A,loading}}}{R}=\alpha\cdot k_{\mathrm{DS}} \quad (11)$$

where α is the coefficient. For the largest energy dissipation, α = 1. The stiffness k_{DS} and force f_{Max} are calculated as

$$\begin{aligned} &\frac{f_{\mathrm{Max}}-f_{\mathrm{A,loading}}}{R}\cdot R+k_{\mathrm{DS}}\left(\Delta_{\mathrm{Max}}-\Delta_{\mathrm{A,loading}}\right) \\ &=k_{\mathrm{DS}}\left(\alpha R+\Delta_{\mathrm{Max}}-\Delta_{\mathrm{A,loading}}\right)=F_{\mathrm{Max}}-F_{\mathrm{A,loading}} \end{aligned} \quad (12)$$

(5) Determine the type and combination of the disc springs according to the calculation results of force P, stiffness k_{DS} and deformation ratio Δ_{Max}-$\Delta_{\mathrm{A,loading}}$. The design parameters of the inner and outer tubes need to satisfy the requirements of the inner and outer diameters of the disc springs.

(6) Determine the design parameters of the piston, permanent magnets and cylinder according to the calculation results of forces f_{Max} and $f_{\mathrm{A,loading}}$, and region R, which are calculated by Eq. (1), as described by Xu *et al.* (2018).

(7) Determine the design parameters of the inner and outer tubes using Eqs. (4)-(8), where ε_n is given as

$$\varepsilon_n=\frac{\varepsilon_{\mathrm{y}}}{\beta} \quad (13)$$

where ε_{y} is the yield strain of steel. The local compression, tension and shear performances of the brace should conform to the code requirements.

After these seven steps, the designed VD–SCB should exhibit a full quasi-flag-shaped hysteretic curve with reliable mechanical behavior. When the brace is used in structures, the maximum bearing capacity of the brace is usually 1000 to 2000kN. As outlined in the design procedure, an outer tube with a dimension of $\phi 250 \times 10$ can meet the bearing capacity requirement. Thus, suitable braces can be easily designed for practical applications.

6. Conclusions

In this study, the force-deformation behavior, strain distribution and failure modes of the VD–SCB are theoretically analyzed, experimentally studied, and numerically simulated to guide the design of the brace. The working principle is explained by describing the working stages and key feature points of the hysteretic curve. The force-deformation behavior of the VD–SCB is divided into seven parts. A large-scale brace specimen was tested under different sinusoidal excitations to analyze its recentering capability and energy dissipation. Results demonstrate that the VD–SCB exhibits a full quasi-flag-shaped hysteretic curves, high ultimate bearing capacity, low activation force and residual deformation, and excellent recentering and energy dissipation capabilities. The average values of the activation force and activation deformation ratio of the brace are 245 kN and 0.34% in compression, 232 kN and 0.55% in tension, respectively. The bearing capacities are 320 kN at a compression deformation ratio of 1.85% and 295 kN at a tension deformation ratio of 1.75%. The residual-deformation energy dissipation of the brace is less than 7.5%.

Equations governing the strain distribution of the VD–SCB are proposed and verified by experimental data and numerical simulated results. Under normal circumstances, the spring blocking plates of the brace yield, resulting in failure. The brace is ultimately damaged when the deformation ratio is 3.30% and the ultimate bearing capacity is 1205 kN. The spring blocking plates can be easily replaced to restore the normal operating conditions of the brace. An unexpected failure mode occurs in the 41st cycle of testing. The clamp of the outer tube is damaged, resulting in the loss of bearing capacity of the brace. This type of failure mode should be avoided in practical

applications. A brief description of the design procedure of the VD–SCB is proposed to guide the design of a reliable VD–SCB in seven steps.

Acknowledgments

The writers gratefully acknowledge the partial support of this research by the National Natural Science Foundation of China under Grant No. 51578058, and Beijing Natural Science Foundation of China under Grant No. 8172038.

References

Abou-Elfath, H. (2017), "Evaluating the ductility characteristics of self-centering buckling-restrained shape memory alloy braces", *Smart Mater. Struct.*, **26**(5), 055020.

Chi, P., Guo, T., Peng, Y., Cao, D. and Dong, J. (2018), "Development of a self-centering tension-only brace for seismic protection of frame structures", *Steel Compos. Struct., Int. J.*, **26**(5), 573-582.

Choi, E., Youn, H., Park, K. and Jeon, J.S. (2017), "Vibration tests of precompressed rubber springs and a flag-shaped smart damper", *Eng. Struct.*, **132**, 372-382.

Chou, C.C. and Chung, P.T. (2014), "Development of cross-anchored dual-core self-centering braces for seismic resistance", *J. Constr. Steel Res.*, **101**, 19-32.

Chou, C.C. and Chung, P.T. (2015), "Development of steel dual-core self-centering braces: quasi-static cyclic tests and finite element analyses", *Earthq. Spectra*, **31**(1), 141208072728004.

Chou, C.C., Tsai, W.J. and Chung, P.T. (2016), "Development and validation tests of a dual-core self-centering sandwiched buckling-restrained brace (SC-SBRB) for seismic resistance", *Eng. Struct.*, **121**, 30-41.

Christopoulos, C., Tremblay, R., Kim, H.J. and Lacerte, M. (2008), "Self-centering energy dissipative bracing system for the seismic resistance of structures: development and validation", *J. Struct. Eng.*, **134**(1), 96-107.

Eatherton, M.R., Fahnestock, L.A. and Miller, D.J. (2014), "Computational study of self-centering buckling-restrained braced frame seismic performance", *Earthq. Eng. Struct. D.*, **43**(13), 1897-1914.

Erochko, J., Christopoulos, C. and Tremblay, R. (2015a), "Design and testing of an enhanced-elongation telescoping self-centering energy-dissipative brace", *J. Struct. Eng.*, **141**(6), 04014163.

Erochko, J., Christopoulos, C. and Tremblay, R. (2015b), "Design, testing, and detailed component modeling of a high-capacity self-centering energy-dissipative brace", *J. Struct. Eng.*, **141**(8), 04014193.

Kitayama, S. and Constantinou, M.C. (2016), "Seismic response analysis of single-degree-of-freedom yielding structures with fluidic self-centering systems", *Eng. Struct.*, **125**, 266-279.

Ma, H. and Yam, M.C.H. (2011), "Modeling of a self-centering damper and its application in structural control", *J. Constr. Steel Res.*, **67**(4), 656-666.

McCormick, J., Aburano, H., Ikenaga, M. and Nakashima, M. (2008), "Permissible residual deformation levels for building structures considering both safety and human elements", *Proceedings of the 14th World Conference on Earthquake Engineering*, Bejing, China.

Miller, D.J., Fahnestock, L.A. and Eatherton, M.R. (2012), "Development and experimental validation of a nickel-titanium shape memory alloy self-centering buckling-restrained brace", *Eng. Struct.*, **40**, 288-298.

Ozbulut, O.E. and Hurlebaus, S. (2012), "Application of an SMA-based hybrid control device to 20-story nonlinear benchmark building", *Earthq. Eng. Struct. D.*, **41**(13), 1831-1843.

Wang, H., Nie, X. and Pan, P. (2017), "Development of a self-centering buckling restrained brace using cross-anchored pre-stressed steel strands", *J. Constr. Steel Res.*, **138**, 621-632.

Xie, Q., Zhou, Z., Huang, J.H. and Meng, S.P. (2016), "Influence of tube length tolerance on seismic responses of multi-storey buildings with dual-tube self-centering buckling-restrained braces", *Eng. Struct.*, **116**, 26-39.

Xu, L.H., Fan, X.W. and Li, Z.X. (2016a), "Development and experimental verification of a pre-pressed spring self-centering energy dissipation brace", *Eng. Struct.*, **127**, 49-61.

Xu, L.H., Fan, X.W., Lu, D.C. and Li, Z.X. (2016b), "Hysteretic behavior studies of self-centering energy dissipation bracing system", *Steel Compos. Struct., Int. J.*, **20**(6), 1205-1219.

Xu, L.H., Xie, X.S. and Li, Z.X. (2018), "Development and experimental study of a self-centering variable damping energy dissipation brace", *Eng. Struct.*, **160**, 270-280.

Zhou, Z., He, X.T., Wu, J., Wang, C.L. and Meng, S.P. (2014), "Development of a novel self-centering buckling-restrained brace with BFRP composite tendons", *Steel Compos. Struct., Int. J.*, **16**(5), 491-506.

CC